A Criterion of the Critical Threshold of the Maximum Shear Stress in Bulk Metallic Glasses with Cryogenic Thermal Cycling by Statistics in Nanoindentation

H. Zhang[1], Z. Wang[1], P. K. Liaw[2], and J.W. Qiao[1, 3, *]

[1]*College of Materials Science and Engineering, Taiyuan University of Technology, Taiyuan 030024, China*

[2] *Department of Materials Science and Engineering, The University of Tennessee, Knoxville, TN, 37996-2200, USA*

[3]*Key Laboratory of Interface Science and Engineering in Advanced Materials, Ministry of Education, Taiyuan University of Technology, Taiyuan 030024, China*

[*]*Corresponding author. E-mail address: qiaojunwei@gmail.com (J.W. Qiao).*

ABSTRACT

Bulk-metallic glasses, BMGs, have different activation volumes by the cryogenic thermal cycling, CTC, treatment. Nanoindentation experiments were carried out in a load-controlled loading mode, and the critical threshold of the maximum shear stress, $(\tau_{max})_C$, was obtained by the noise-reduction procedures and the statistical analysis. The activation volume, V^*, was gained from the nonlinear slope by introducing a first-order polynomial. Based on the mean-filed theory, MFT, a universal criterion is successfully established, $(\tau_{max})_C = V^{*-\lambda}$, where $\lambda = 0.30 \pm 0.10$. According to many previous studies on $(\tau_{max})_C$ and V^* of metallic glasses, MGs, three applicable conditions of the universal criterion are extracted.

Keywords

Bulk-metallic glasses; Cryogenic thermal cycling treatment; Nanoindentation; Mean-field theory; Universal criterion

INTRODUCTION

Bulk-metallic glasses (BMGs) are novel alloys with unique mechanical properties for potential structural applications [1-3]. Over the past several decades, the plastic-deformation mechanism of BMGs has been widely investigated [4, 5]. The shear-transformation zones (STZs) are fatally significant in understanding the irreversible deformation of BMGs [6]. The activation and evolution of STZs play a primary role in the shear-banding events and instantaneous mechanical response [7]. Based on Schuh and Lund's work, the activation volume, V^*, and the size of STZs can be estimated through the statistical method, which relies on the cumulative distribution of the maximum shear stress, τ_{max} [8]. These parameters have been widely studied in different treatments and various experimental environments for BMGs with diverse systems by nanoindentation tests [9-28]. To better understand the microscopic plastic-deformation behavior of BMGs, the correlations of these parameters are urgently needed by appropriate methods [29, 30].

It is known that the cryogenic thermal cycling, CTC, of BMGs is easily applied, and gives changes in V^* to improve their compressive plasticity [31, 32]. Therefore, the samples with different V^* in Zr-based BMGs can be achieved through different CTC cycles to conduct the nanoindentation study [33, 34]. According to the Oliver and Pharr approach, the value of τ_{max} can be computed for these samples by the noise-reduction procedures and the statistical analysis [35]. The values of V^* were obtained from the nonlinear slope by introducing a low-order polynomial [17]. Then, it is clearly found that the range of τ_{max} and the critical threshold of the maximum shear

stress, $(\tau_{max})_C$, all decrease with the increasement of V^*. Dahmen *et al*. developed an analytical mean-field theory, MFT model, which yields a new phase diagram for the avalanche statistics of sheared granular materials [36]. Luo *et al*. concluded a universal criterion for the failure threshold in slowly sheared BMGs according to the MFT [37]. Here, a new universal criterion is successfully established by introducing the MFT, $(\tau_{max})_C = V^{*-\lambda}$, where $\lambda = 0.30 \pm 0.10$. Meanwhile, a series of previous works on $(\tau_{max})_C$ and V^* of metallic glasses, MGs, were summarized in the form of a chart, and three applicable conditions of the universal criterion are extracted.

EXPERIMENTAL

The Zr-based BMG ($Zr_{58}Cu_{22}Fe_8Al_{12}$, atomic percent, at%) ingots were prepared by arc melting the mixture of high-purity (above 99.9% volume or weight percent?) constituent metals in a water-cooled copper crucible under a high-purified argon atmosphere obtained by melting a pure titanium. Rectangular plates ($10\ \text{mm} \times 2\ \text{mm} \times 2\ \text{mm}$) were cut from these ingots and all double grinded and polished to an identical thickness (~ 1.9 mm). During the CTC treatment, the selected plates were first dipped into liquid nitrogen for 1 min. and then immersed in a 373 K constant-temperature water bath for 1 min. called one complete cycle. The post-treated plates after 0, 100, and 400 cycles were denoted as UC (unchanged), CTC100, and CTC400, respectively. These fully glass structures were examined, using X-ray diffraction with Co-Kα radiation and scanning from 20° to 100° at the scanning speed of 5°/min.

Nanoindentation (Bruker, Minneapolis, MN, USA) tests were conducted at

room temperature with a Berkovich diamond indenter. The displacement and load resolutions of the machine were, respectively, less than 0.01 nm and 50 nN, respectively. Before testing, the instrument was calibrated, employing the standard fused silicon to ensure thermal stability for at least 30 min., until the thermal drift was below 0.05 nm $\bullet s^{-1}$. The tests were conducted under a load-control mode, and loaded to a maximum load of 5 mN at a 1 mN/s loading rate with a fixed holding time of 2 s, followed by a decline to zero at the rate of 1 mN/s. Around 100 tests were conducted for each sample in order to obtain statistically significant data set from the applied load (P) and penetration depth (h) curve.

RESULTS

Figure 1(a) shows the representative loading-displacement (P-h) curves for the indentation on the three CTC treatment specimens. The curves were presented on a single graph by moving them along the displacement axis. A series of sudden displacement bursts can clearly be observed, which manifest as serrated flows or "pop-ins" in the P-h curves, as indicated by the purple arrow in Fig. 1(a), associated with the formation and propagation of shear bands [38, 39]. In addition, the nano-hardness of the samples is generally decreased as the CTC is increased, which can be attributed to the increasing concentration of free volumes, as displayed in the inset of Fig. 1(a) [40, 41].

The above experimental results clearly demonstrate that the deformation behavior and mechanical properties of the three samples are closely related to the CTC treatment. This trend was caused by the CTC treatment, which resulted in material

softening and relaxation within the internal structure of BMG samples. It is well known that the plastic deformation of BMGs at room temperature is concentrated in a narrow region, such as flow defects or STZs, and the latter has a great influence on the plastic behavior of BMGs [6]. STZs are not structural defects but the structural change processes at the beginning of straining in BMGs [42]. The calculation of the correlation between the STZ volume and properties of BMGs via experimentation have been extensively studied [9-18]. In order to estimate the STZ volume, the statistical analysis is required on the shear-stress data derived from serrations [19-28].

Prior to the statistical analysis of the shear stress, the effective serrations are first needed to be extracted from the *P-h* curves. Therefore, the noise-reduction procedures must be employed to remove a large amount of noise serrations to ensure the accuracy of the statistical analysis [43]. For example, in the case of UC, the initial curve of the displacement derivative variation with time (*dh/dt-t*) was obtained, and the curve fitting for *dh/dt-t* was performed, as shown by the solid black line in Figure 1(b). Here, an exponential function was used to fit the *dh/dt-t* curve. The exponential function is described as follows [43]

$$\frac{dh}{dt} = C \cdot [exp(A \cdot t^B) - 1] + D, \quad (1)$$

where A, B, C, and D are the fitting parameters. Subsequently, the fitted values were subtracted from the raw data, and the differences were marked as the processed data. A linear regression equation was fitted again to the curve of the processed data versus time. The fitting equation is [43]

$$\frac{dh}{dt} = K \cdot t + M, \quad (2)$$

where M is the fitting parameter. Repeating the above step until the slope (K) of Eq. (1), K, was close to zero. The purpose of this stage is to remove the effect of the increasing indentation displacement, which affects the accuracy of statistics on the raw data of the time derivative of displacement. Then, the median of the processed data of the time derivative of displacement is calculated, and moved to the position of zero, as displayed in the set of Fig. 1(b). It is well known that if there are no serrations, the background noise will follow a Gauss distribution. Thus, the Gauss fit was separately performed to the processed data on both sides of the median. The Gauss fit equation is [43]

$$N = a + \frac{b}{g\sqrt{\pi/2}} exp\left(-2\left(\frac{x}{g}\right)^2\right), \quad (3)$$

where a, b, and g are fitting parameters, and N represents the cumulative distribution of the processed data value. Based on the difference between the fitting curves on both sides of the median, the critical background noise value of 37 nm/s was determined at a 1 mN/s loading rate in the case of UC.

As exhibited in Figure 1(c), the influence of the background noise is eliminated, and the serrations are identified accurately. The serrations (the strain bursts) during the loading process of the constant load generally correspond to the plastic deformation because the indentation cannot be recovered. Therefore, they can be considered as a transition from the instantaneous elastic strain to plastic deformation, which are like????? to the first pop-in under each loading of the spherical indenter [18, 24]. Here, the estimation of the shear stress is determined by the first pop-in under each loading of the Berkovich-diamond indenter [17].

In BMGs, the shear stress, τ, is relevant to the indention hardness, H, during nanoindentation, described as $\tau = H/3\sqrt{3}$ [7]. For the Berkovich indenter, the hardness, H, is calculated by the Oliver and Pharr approach [35], $H = P/24.56h_C^2$, where h_C is the contact depth obtained from the load-depth curve, $h_C = h - \varepsilon P/S$. Then τ can be determined by the following equation,

$$\tau = \frac{P}{24.56\times3\times\sqrt{3}\cdot(h-\varepsilon\cdot P/S)^2}. \quad (4)$$

where $\varepsilon = 0.75$ is a constant, and the contact stiffness, S, is obtained from the slope of the unloading curve at the peak load. In Figure 1(d), the effect of the CTC is clearly apparent that the average value and the variance of τ_{max} decreases with increasing the CTC, which can promote the increasement of free volumes in BMGs.

The cumulative-probability distributions of τ_{max} in the three BMGs were illustrated in Figure 2(a). Based on Schuh and Lund's work [8], the yield strength is affected by the thermally-assisted and stress-biased processes, which may cause it to fluctuate within a certain range. This trend is ascribed to that the thermal noise sometimes favors yielding and works against it at other times. Hence, the cumulative distribution function, f, of first pop-in events can be described as a function of τ beneath the indenter in terms of,

$$f = 1 - exp\left[-\frac{kT\dot{\gamma}_0}{V^*(d\tau/dt)}exp\left(-\frac{\Delta F^*}{kT}\right)exp\left(\frac{\tau V^*}{kT}\right)\right], \quad (5)$$

where kT is the thermal energy (k is the Boltzmann constant, and T is the temperature), $\dot{\gamma}_0$ is the attempt frequency, $d\tau/dt$ is a constant in the fixed loading rate-control mode, ΔF^* is the Helmholtz activation energy, and V^* is the activation volume. V^* can be calculated by calculating the slope of $ln[ln(1-f)^{-1}]$ versus τ curve, with Eq. (5)

rewritten as

$$ln[ln(1-f)^{-1}] = \left\{\frac{\Delta F^*}{kT} + ln\left[\frac{kT}{V^*\left(\frac{d\tau}{dt}\right)}\right]\right\} + \left(\frac{V^*}{kT}\right)\tau. \quad (6)$$

A linear relationship clearly does not exist in the correlations between the $ln[ln(1-f)^{-1}]$ and τ_{max} for the three BMGs, as exhibited in Figure 2(b), which has been confirmed in previous results [14]. Considering that the elastic-plastic transition deformation process of the tested BMGs was a thermally-activated process, the activation volume should be related to the local shear stress, which might be responsible for this nonlinear relationship [17]. To account for the observed nonlinearity, Eq. (6) is modified by introducing a first-order polynomial

$$V^*(\tau) = V_0 + V_1\tau, \quad (7)$$

where V_0 and V_1 are fitting parameters.

Once the V^* is determined, the shear transformation zone (STZ) volume, the most fundamental internal flow unit size for plastic flows in the BMGs, can be estimated by the cooperative shear model (CSM) of Johnson and Samwer [44]. The STZ volume, Ω, is

$$\Omega = \frac{\tau_0}{6R_0G\gamma_C^2\zeta(1-\tau/\tau_0)^{\frac{1}{2}}}V^*, \quad (8)$$

where G is the shear modulus (32.5 GPa for the BMG under consideration here [24]), γ_C is the critical shear strain ($\gamma_C = \tau/G$), and τ and τ_0 are, respectively, the threshold shear strengths at T and 0 K. $R_0 \approx 1/4$ and $\zeta \approx 3$ are constants. For the average elastic limit, $\gamma_C \approx 0.027$, $\tau_0/G = 0.036$, and the value of τ/τ_0 can be estimated from the constitutive equation,

$$\gamma_C = \tau/G = \gamma_{C0} - \gamma_{C1}\left(T/T_g\right)^{2/3}, \quad (9)$$

where $\gamma_{C0} = 0.036 \pm 0.002$, $\gamma_{C1} = 0.016 \pm 0.002$, G has a weak temperature dependency for BMGs, and T_g is the glass-transition temperature (677 K [45]). Once the STZ volume is determined, the number of atoms in a STZ, N, can be obtained according to the dense-packing hard-sphere model in BMGs Please give references, wherein the average atomic radius of $R = (\sum_i^n A_i r_i^3)^{\frac{1}{3}}$, A_i and r_i are the atomic fraction and atomic radius of each element, respectively [46]. The activation volume, the STZ volume, and the number of atoms in a STZ of the three BMGs were listed in Table 1.

The larger volume and size of the STZ means that more free volumes are introduced into the alloys, resulting in an increment of the interatomic spacing and a reduction of the bonding strength between atoms [47, 48]. During the CTC treatment, the formation of the denser atomic packing broadened the energy barrier distribution to increase the elastic fluctuations, and the atomic motion produced more contents of free volumes in the loose-packed regions [34]. If enough free volumes reach a critical value, a main connected cluster will form in the STZ, which leads to the creation of a single STZ, and when many STZs are present, they together evolve into a mature shear band [18]. In the present study, the CTC treatment increased the STZ volume and the number of atoms of the BMGs, and a larger STZ volume initiation causes a more intense stress concentration. Compared with a small STZ volume, a larger STZ volume can induce fewer STZs activations to form a shear-band nucleus [33, 49]. STZs with a larger volume lead to the easy generation and multiplication of shear bands, and increase the shear-band density, plastic zones, and plasticity [18, 41].

DISCUSSION

It is entirely appropriate to convert the cumulative probability into the complementary cumulative distribution function (CCDF) to analyze the universal criterion of the maximum shear stress under different CTC treatments. Here, using the different activation volumes to quantify the different CTC treatments. The CCDF, $C(\tau_{max}, V^*)$, for the magnitudes of maximum shear stress under different activation volumes are drawn in Fig. 3(a). It gives that the probability of observing a magnitude larger than τ_{max} is [50]

$$C(\tau_{max}, V^*) = V^{*\lambda(\kappa-1)} C'\left(\tau_{max} V^{*\lambda}\right) \tag{10}$$

where $\tau_{max} V^{*\lambda}$ is an independent variable, and $C'\left(\tau_{max} V^{*\lambda}\right)$ is a universal scaling function, which is depicted by the green dotted line in Figure 3(b). The experimental critical threshold, $(\tau_{max})_C$, decreases quite significantly with increasing the activation volume, as shown in the inset of Fig. 3(a). λ is the constant in MFT and roughly determined by [37, 50]

$$(\tau_{max})_C = a V^{*-\lambda}, \tag{11}$$

where, $a \approx 1$ and $\lambda = 0.30 \pm 0.10$ can be obtained by fitting. Under the guidance of the MFT and with the help of normalization, $\lambda = 0.32 \pm 0.01$ and $\kappa = 1.49 \pm 0.01$ of the scaling can be accurately determined in this experimental environment. The value of κ is basically consistent with the MFT prediction ($\kappa = 1.5$), within the error range [36, 51]. However, the scaling exponent, λ, deviates from the MFT prediction, because the maximum shear stress was taken from the elastoplastic-transition process, i.e., the plastic-flow-instability state [50]. So far, it can be concluded that the critical threshold of the maximum shear stress of Zr-based BMGs is controlled by the activation volume

in this experimental environment, and it follows a universal criterion of Eq. (11).

In order to rule out the possibility that Zr-based BMGs have particularity in this study, it is further verified whether the present established universal criterion is suitable to all BMGs. Firstly, the critical threshold of the maximum shear stress, $(\tau_{max})_C$, and the corresponding activation volume, V^*, are listed in Table 1 about various MGs with different samples, treatments, indenters and test modes [9-28]. Then, these two parameters are plotted in the form of abscissa and ordinate in Figure 4, respectively. And in the light of the correlation of the component, these MGs are divided into 20 systems. It is clearly found that most systems are suitable for the universal criterion in their respective experimental environment. According to the relevance of the experimental environment, these systems that do not meet at all and partially meet the universal criterion are regarded as regions I-IV and V-VII, respectively. We summarize some reasons why MGs do not satisfy the universal criterion in these regions. Firstly, the activation volume of thin film MGs and ribbon MGs are larger than that of BMGs with the same components due to the differences in the fabrication process of the samples [52]. In region I, the two thin film MGs and one ribbon MG do not fulfill the universal criterion is attributed to the high activation volume of their original samples [9, 10]. Coincidentally, most of the remaining thin film MGs and ribbon MGs mentioned in Table 1 are located right on the edge of the universal criterion. Secondly, because the test mode is controlled by the displacement in region II, BMGs do not content the universal criterion [26, 27]. While the test mode of other BMGs is under a load control in the same system and other systems [9-25, 28]. Thirdly, in the calculation

of the activation volume of the BMGs in regions III and IV, the nonlinearity of the slope of $ln[ln(1-f)^{-1}]$ versus τ_{max} curve is explained by introducing a second-order polynomial [14, 17]. It is found that the higher the order and the larger the activation volume by adopting a polynomial to solve the nonlinear phenomenon. Thus, it is best to understand the nonlinear phenomenon through applying the first-order polynomial (Eq. (7)). Fourth, the phenomenon that the regions V-VII do not partly meet the universal criterion is attributed to the deviation of the experimental and analytical procedures.

It can be concluded that the universal criterion is $(\tau_{max})_C = V^{*-\lambda}$, where $\lambda = 0.30 \pm 0.10$. The applicable conditions: (1) the samples are BMGs rather than thin-film MGs and ribbon MGs; (2) the test mode is under a load control rather than displacement control; (3) the nonlinearity of the slope of $ln[ln(1-f)^{-1}]$ versus τ_{max} curve is settled, using the first-order polynomial [Eq. (7)]. Therefore, when MGs satisfy the three conditions, even if various BMGs have different shapes and treatments of bulk samples, indenters, maximum loads, and loading speeds of the load-control mode, the critical threshold of the maximum shear stress and the activation volume only fluctuate within the universal criterion.

CONCLUSION

In this study, three samples of Zr-based BMGs were gained with different activation volumes by a CTC treatment, and nanoindentation experiments were performed in a load-controlled loading mode. Firstly，the values of the activation volumes of the three samples were obtained through the noise-reduction procedures and

the statistical analysis, where the nonlinearity of the slope of $ln[ln(1-f)^{-1}]$ versus τ_{max} curve is solved by introducing the first-order polynomial [Eq. (7)]. Then, according to the mean field theory, the universal criterion for the critical threshold of the maximum shear stress of BMGs by statistics was successfully established, $(\tau_{max})_C = V^{*-\lambda}$, where $\lambda = 0.30 \pm 0.10$. Finally, combined with the previous work of $(\tau_{max})_C$ and V^* about MGs, three applicable conditions of the universal criterion are summarized.

Acknowledgement

J.W.Q. would like to acknowledge the financial support of the National Natural Science Foundation of China (No. 52071229). P.K.L. very much appreciates the supports from the National Science Foundation (DMR – 1611180, 1809640, and 2226508) with program directors, Drs. J. Madison, J. Yang, G. Shiflet, and D. Farkas .

REFERENCES

[1] M.M. Trexler, N.N. Thadhani, Progress in Materials Science 55(8) (2010) 759-839.
[2] W.H. Wang, Progress in Materials Science 57(3) (2012) 487-656.
[3] Y.Q. Cheng, E. Ma, Progress in Materials Science 56(4) (2011) 379-473.
[4] F. Spaepen, Acta Metall 25 (1977) 407-415.
[5] H. Zhang, Z. Wang, H.J. Yang, X.H. Shi, P.K. Liaw, J.W. Qiao, Scripta Materialia 222 (2023).
[6] A.S. Argon, Acta Metallurgica 27(1) (1979) 47-58.
[7] C.A. Schuh, T.G. Nieh, Journal of Materials Research 19(1) (2004) 46-57.
[8] C.A. Schuh, A.C. Lund, Journal of Materials Research 19(7) (2004) 2152-2158.
[9] Y. Ma, G.J. Peng, T.T. Debela, T.H. Zhang, Scripta Materialia 108 (2015) 52-55.
[10] Y. Ma, J.H. Ye, G.J. Peng, D.H. Wen, T.H. Zhang, Materials Science and Engineering: A 627 (2015) 153-160.
[11] R. Limbach, K. Kosiba, S. Pauly, U. Kühn, L. Wondraczek, Journal of Non-Crystalline Solids 459 (2017) 130-141.
[12] K. Tao, J.C. Qiao, Q.F. He, K.K. Song, Y. Yang, International Journal of Mechanical Sciences 201 (2021).
[13] Y. Ma, G.J. Peng, Y.H. Feng, T.H. Zhang, Materials Science and Engineering: A 651 (2016) 548-555.
[14] D. Tönnies, K. Samwer, P.M. Derlet, C.A. Volkert, R. Maaß, Applied Physics Letters 106(17) (2015).
[15] G.K. Liao, Z.L. Long, M.S.Z. Zhao, L. Peng, W. Chai, Z.H. Ping, Physica B: Condensed Matter 534 (2018) 163-168.
[16] P. Saini, R.L. Narayan, Journal of Alloys and Compounds 898 (2022).
[17] F. Dong, Y. Chu, M. He, Y. Zhang, W. Li, P.K. Liaw, B. Wang, L. Luo, Y. Su, R.O. Ritchie, X. Yuan, Journal of Materials Science & Technology 102 (2022) 36-45.
[18] F. Dong, M. He, Y. Zhang, B. Wang, L. Luo, Y. Su, H. Yang, X. Yuan, Materials Science and Engineering: A 759 (2019) 105-111.
[19] Z.Q. Chen, L. Huang, P. Huang, K.W. Xu, F. Wang, T.J. Lu, Materials Science and Engineering: A 677 (2016) 349-355.
[20] Y. Li, K. Zhang, Y. Wang, W. Tang, Y. Zhang, B. Wei, Z. Hu, Materials Science and Engineering: A 773 (2020).
[21] Y. Zhao, I.-C. Choi, M.-Y. Seok, M.-H. Kim, D.-H. Kim, U. Ramamurty, J.-Y. Suh, J.-i. Jang, Acta Materialia 78 (2014) 213-221.
[22] Q.P. Cao, J.B. Jin, Y. Ma, X.Z. Cao, B.Y. Wang, S.X. Qu, X.D. Wang, D.X. Zhang, J.Z. Jiang, Journal of Non-Crystalline Solids 412 (2015) 35-44.
[23] I.-C. Choi, Y. Zhao, B.-G. Yoo, Y.-J. Kim, J.-Y. Suh, U. Ramamurty, J.-i. Jang, Scripta Materialia 66(11) (2012) 923-926.
[24] I.-C. Choi, Y. Zhao, Y.-J. Kim, B.-G. Yoo, J.-Y. Suh, U. Ramamurty, J.-i. Jang, Acta Materialia 60(19) (2012) 6862-6868.
[25] X.L. Bian, D. Zhao, J.T. Kim, D. Şopu, G. Wang, R. Pippan, J. Eckert, Materials Science and Engineering: A 752 (2019) 36-42.
[26] T. Liu, Y. Gao, H. Bei, AIP Advances 7(8) (2017).

[27] W. Li, Y. Gao, H. Bei, Sci Rep 5 (2015) 14786.
[28] Y. Tong, J.C. Qiao, J.M. Pelletier, Y. Yao, Journal of Alloys and Compounds 785 (2019) 542-552.
[29] S.T. Liu, Z. Wang, H.L. Peng, H.B. Yu, W.H. Wang, Scripta Materialia 67(1) (2012) 9-12.
[30] C.A. Schuh, T.G. Nieh, Acta Materialia 51 (2003) 87-99.
[31] S.V. Ketov, Y.H. Sun, S. Nachum, Z. Lu, A. Checchi, A.R. Beraldin, H.Y. Bai, W.H. Wang, D.V. Louzguine-Luzgin, M.A. Carpenter, A.L. Greer, Nature 524(7564) (2015) 200-3.
[32] Y. Tang, H. Zhou, H. Lu, X. Wang, Q. Cao, D. Zhang, W. Yang, J.Z. Jiang, Nat Commun 13(1) (2022) 2120.
[33] W. Guo, R. Yamada, J. Saida, Intermetallics 93 (2018) 141-147.
[34] Y. Zhu, Y. Zhou, A. Wang, H. Li, H. Fu, H. Zhang, H. Zhang, Z. Zhu, Materials Science and Engineering: A 850 (2022).
[35] W.C. Oliver, G.M. Pharr, Journal of Materials Research 7(6) (1992) 1564-1583.
[36] K.A. Dahmen, Y. Ben-Zion, J.T. Uhl, Nature Physics 7(7) (2011) 554-557.
[37] Y.S. Luo, Z. Wang, J. Eckert, J.W. Qiao, Journal of Applied Physics 129(15) (2021).
[38] Y. Zhang, J.P. Liu, S.Y. Chen, X. Xie, P.K. Liaw, K.A. Dahmen, J.W. Qiao, Y.L. Wang, Progress in Materials Science 90 (2017) 358-460.
[39] L. Cheng, Z.M. Jiao, S.G. Ma, J.W. Qiao, Z.H. Wang, Journal of Applied Physics 115(8) (2014).
[40] N. Li, L. Liu, Q. Chen, J. Pan, K.C. Chan, Journal of Physics D: Applied Physics 40(19) (2007) 6055-6059.
[41] J.W. Lv, F.L. Wang, D.W. Yin, S. Zhang, Z.Q. Cai, Z.L. Shi, M.Z. Ma, X.Y. Zhang, Journal of Alloys and Compounds 887 (2021).
[42] M. Chen, Annual Review of Materials Research 38(1) (2008) 445-469.
[43] G. Liao, Z. Long, M. Zhao, M. Zhong, W. Liu, W. Chai, Journal of Non-Crystalline Solids 460 (2017) 47-53.
[44] W.L. Johnson, K. Samwer, Phys Rev Lett 95(19) (2005) 195501.
[45] K. Mondal, T. Ohkubo, T. Mukai, K. Hono, Materials Transactions 48(6) (2007) 1322-1326.
[46] J.D. Bernal, Nature 185 (1960) 68-70.
[47] W.H. Jiang, F.X. Liu, Y.D. Wang, H.F. Zhang, H. Choo, P.K. Liaw, Materials Science and Engineering: A 430(1-2) (2006) 350-354.
[48] L. Liu, K.C. Chan, Materials Letters 59(24-25) (2005) 3090-3094.
[49] D. Pan, A. Inoue, T. Sakurai, M.W. Chen, Proc Natl Acad Sci U S A 105(39) (2008) 14769-72.
[50] J. Antonaglia, X. Xie, G. Schwarz, M. Wraith, J. Qiao, Y. Zhang, P.K. Liaw, J.T. Uhl, K.A. Dahmen, Sci Rep 4 (2014) 4382.
[51] K.A. Dahmen, Y. Ben-Zion, J.T. Uhl, Phys Rev Lett 102(17) (2009) 175501.
[52] M. Li, J. Tan, X.M. Qin, D.H. Lu, Z.X. Feng, C.J. Li, S.V. Ketov, M. Calin, J. Eckert, Journal of Applied Physics 129(8) (2021).

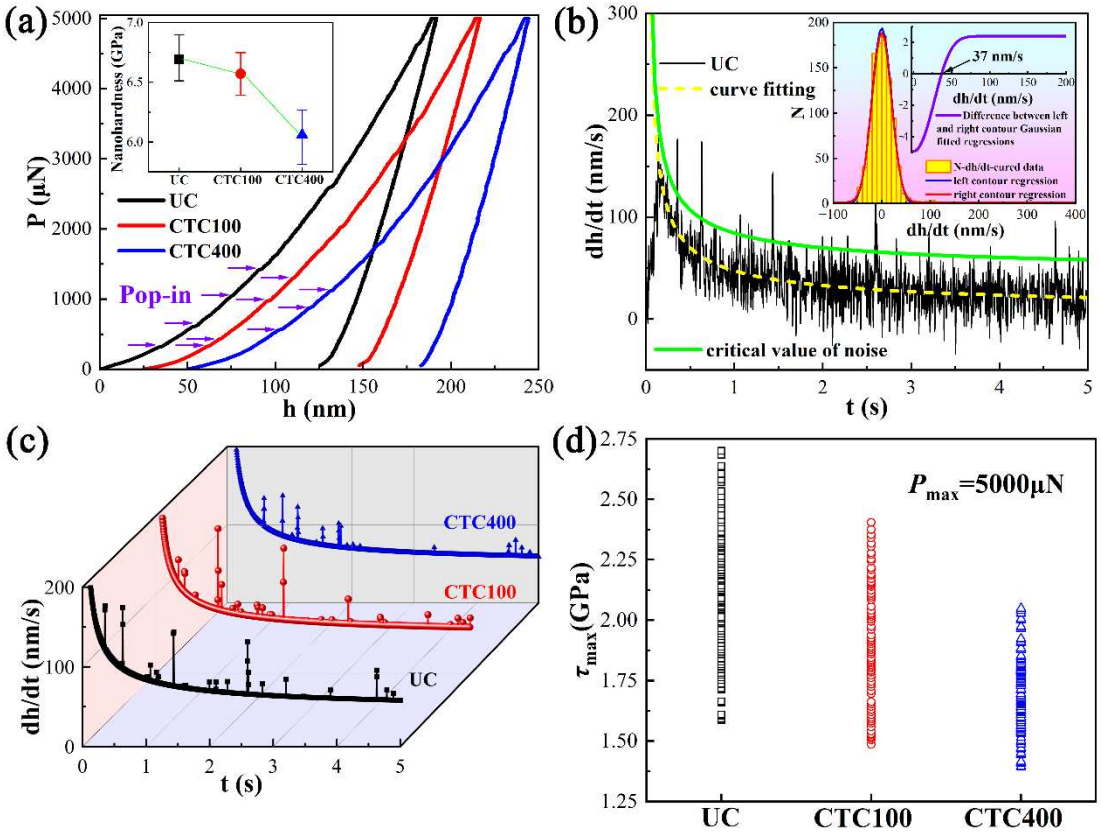

Fig. 1. (a) The representative loading-displacement, *P-h* curves of UC, CTC100, CTC400. The inset shows the variation in the nano-hardness for the three CTC treatment specimens. (b) The initial curve of the displacement-derivative variation with time, dh/dt-t, is indicated by the solid black. The fitted curve and the curve of the critical value about noise are denoted by a yellow dashed and a green solid, respectively. The inset shows that the critical value of the background noise is obtained by the law that it obeys a Gaussian distribution without serrations. (c) The dh/dt-t curves of UC, CTC100, and CTC400 after the noise-reduction procedures. (d) The variation of the maximum shear stress, τ_{max}, determined by the first burst under each dh/dt-t curve.

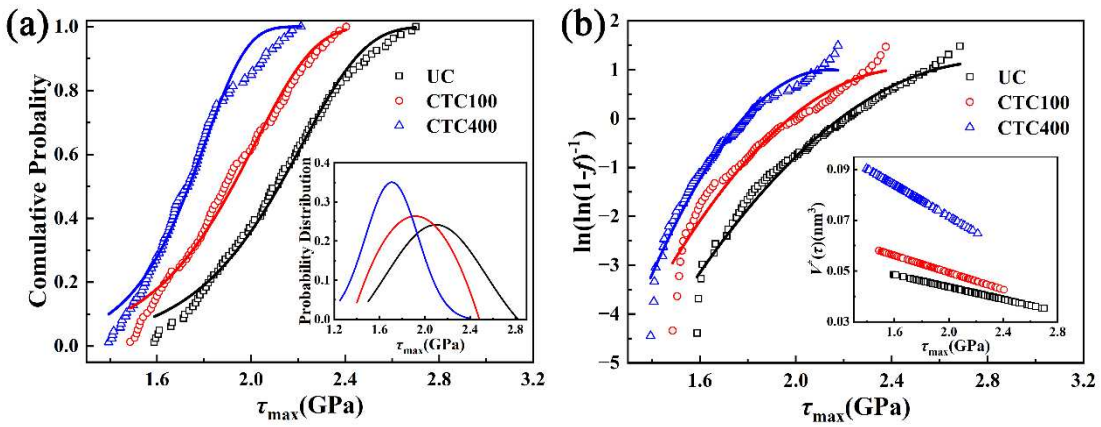

Fig. 2. (a) The cumulative probability distributions of τ_{max} of UC, CTC100, CTC400. The inset shows the probability distributions of τ_{max} for the three CTC-treatment specimens. (b) The correlations between $ln[ln(1-f)^{-1}]$ and τ_{max} of UC, CTC100, CTC400. The nonlinearity of the slope of $ln[ln(1-f)^{-1}]$ versus τ_{max} curve is explained by introducing a first-order polynomial. The inset shows the range of V^* values for the three CTC treatment specimens.

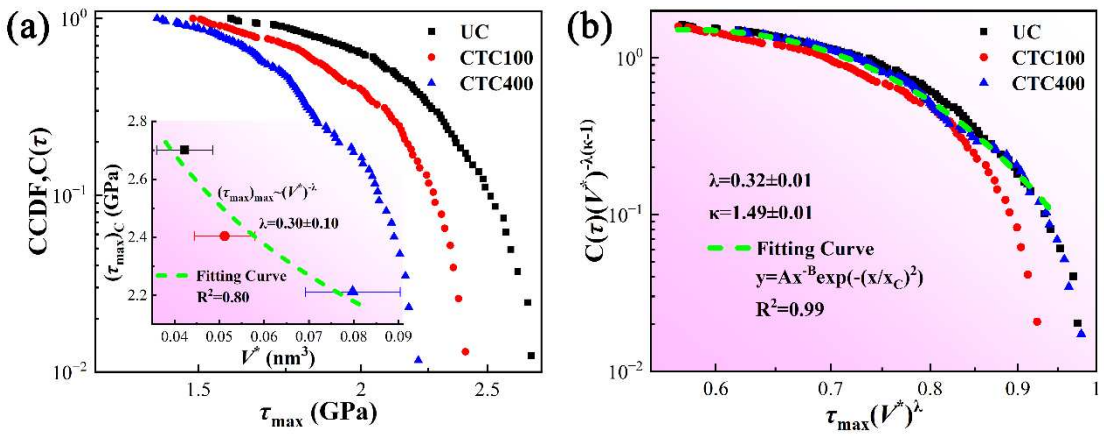

Fig. 3. (a) The complementary cumulative distribution functions, $C(\tau_{max}, V^*) = V^{*\lambda(\kappa-1)} C'(\tau_{max} V^{*\lambda})$, for τ_{max} of UC, CTC100, CTC400. The inset displays the variation of the critical threshold of the maximum shear stress, $(\tau_{max})_C$, vs the activation volume, V^*. The relation, $(\tau_{max})_C = aV^{*-\lambda}$, is obtained by fitting. (b) Rescale of the axes by tuning the exponents, κ and λ, until the curves lie on top of each other to obtain a universal collapse scaling, fitted by a green dashed line. $\lambda = 0.32 \pm 0.01$ and $\kappa = 1.49 \pm 0.01$ are drawn for the collapse.

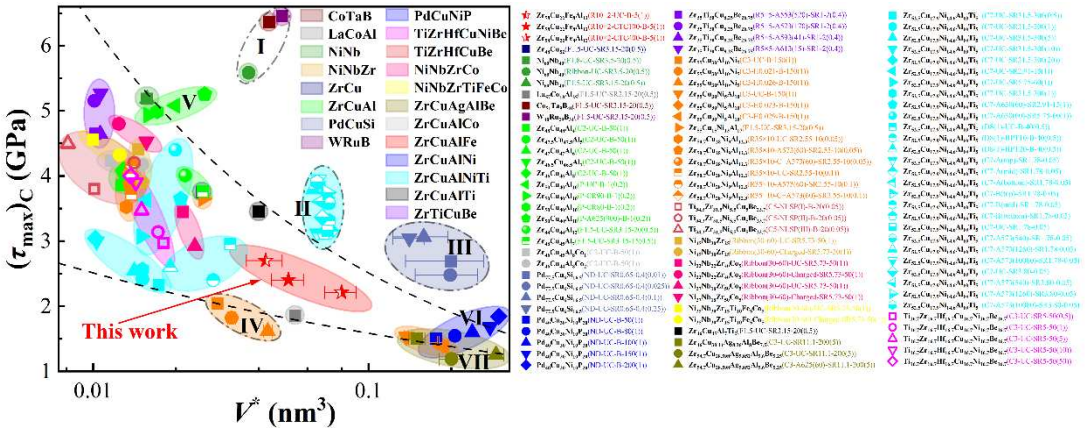

Fig. 4. The critical threshold of the maximum shear stress, $(\tau_{max})_C$, of metallic glasses as a function of the activation volume, V^*. The universal criterion is represented by a central area of the dashed line. The graph includes experimental results from this work and previous studies [9-28]. For details of each symbol on the right, please refer to Table 2.

Table 1

The activation volume, V^*, the STZ volume, Ω, and the number of atoms in a STZ, N for the three CTC-treatment specimens.

	$V^*(\mathrm{nm}^3)$	$\Omega(\mathrm{nm}^3)$	N(atom)
UC	0.0423±0.0063	0.933±0.14	67±10
CTC100	0.0512±0.0068	1.129±0.15	81±11
CTC400	0.0798±0.0106	1.76±0.233	127±17

Table 2

Various BMGs with different samples, treatments, indenters, and test modes. Sample: R, rectangular; F, film; Ribbon, ribbon; C, cylindrical rod; P, plate shape; ND, no description; D, desk. Treatment: UC, un-change; CTC, cryogenic thermal cycling; CR, cold rolled; A, annealed; H, hydrogenation; C, surface-coated; NLSP, nanosecond laser shock peening; Charged, H-charging; HPT, high-pressure torsion. Indenter: B, Brekovich; SR, spherical. Test mode: 5(1), load-control; $0.05s^{-1}$, displacement-control.

BMG	Sample	Treatment	Indenter	Test mode	$(\tau_{max})_C$	V^*	
$Zr_{58}Cu_{22}Fe_8Al_{12}$	R10×2	UC	B	5(1)	2.701	0.0423± 0.0063	This Work
		CTC100			2.405	0.05119± 0.0068	
		CTC400			2.212	0.07977± 0.0106	
$La_{57}Co_{18}Al_{25}$	F1.5	UC	SR3.15	20(0.5)	1.856	0.0541	[9]
$Zr_{48}Cu_{52}$					3.757	0.0249	
$Zr_{44}Cu_{44}Al_{12}$					4.008	0.0216	
$Zr_{55}Cu_{15}Ni_{13}Al_{17}$					3.650	0.0251	
$Ni_{60}Nb_{40}$					5.184	0.0157	
$Co_{51}Ta_9B_{40}$					6.369	0.0435	
$W_{40}Ru_{29}B_{31}$					6.455	0.0485	
$Ni_{60}Nb_{40}$	F1.8 Ribbon	UC	SR3.5	20(0.5)	5.185	0.0157	[10]
$Ni_{60}Nb_{40}$					5.585	0.0367	
$Zr_{48}Cu_{48}Al_4$	C2	UC	B	50（1）	3.859	0.0127	[11]
$Zr_{47.5}Cu_{47.5}Al_5$					3.897	0.0131	
$Zr_{47}Cu_{47}Al_6$					3.962	0.014	
$Zr_{46.5}Cu_{46.5}Al_7$					4.019	0.0128	
$Zr_{46}Cu_{46}Al_8$					4.094	0.0129	
$Zr_{46}Cu_{45}Al_8Co_1$					4.237	0.0116	
$Zr_{46}Cu_{44}Al_8Co_2$					4.172	0.0151	
$Zr_{50}Cu_{40}Al_{10}$	P	UC	B	1（0.2）	5.080	0.0199	[12]
		CR90			4.935	0.0159	
		CR80			4.991	0.0171	
		A625(900)			5.257	0.0254	
$Zr_{48}Cu_{45}Al_7$	F1.5	UC	SR3.15	15(0.5)	3.763	0.025	[13]
$Zr_{46}Cu_{45}Al_7Ti_2$					3.450	0.04	
$Pd_{77.5}Cu_6Si_{16.5}$	ND	UC	SR0.65	0.4(0.01)	2.693	0.1991± 0.063	[14]
				0.4(0.025)	2.479	0.198± 0.0504	

$Pd_{40}Cu_{30}Ni_{10}P_{20}$	ND	UC	B	0.4(0.1)	3.065	0.1586± 0.036	[15]
				0.4(0.25)	3.044	0.1405± 0.0182	
				50(1)	1.498	0.176	
				80(1)	1.546	0.206	
				100(1)	1.598	0.238	
				150(1)	1.680	0.276	
				200(1)	1.843	0.297	
$Zr_{35}Ti_{30}Cu_{8.25}Be_{26.75}$	R5×5	A553(520)	SR1	2（0.4）	4.647	0.010186	[16]
		A573(170)			5.154	0.010114	
		A593(41)			4.647	0.010609	
		A613(15)			5.269	0.010648	
$Zr_{55}Cu_{30}Al_{10}Ni_5$	C3	UC	B	150(1)	2.042	0.02824± 0.0007	[17]
		H0.021			1.822	0.03183± 0.0011	
		H0.026			1.615	0.04304± 0.0016	
$Zr_{55}Cu_{30}Al_{10}Ni_5$	C3	UC	B	150(1)	1.532	0.137± 0.002	[18]
		H0.023			1.445	0.179± 0.0015	
		H0.029			1.372	0.188± 0.0023	
$Zr_{50.7}Cu_{28}Al_{12.3}Ni_9$	R35×10	UC	SR2.55	10(0.05)	3.526	0.0132	[19]
		A573(60)			3.863	0.0136	
		C+A573(60)			4.036	0.0135	
		UC		10(0.1)	3.716	0.0138	
		A573(60)			4.039	0.0137	
		C+A573(60)			4.163	0.0139	
$Ti_{34.3}Zr_{31.5}Ni_{5.5}Cu_5Be_{23.7}$	C5	NLSP(I)	B	20(0.05)	3.798	0.0101	[20]
		NLSP(II)			4.202	0.0141	
		NLSP(III)			4.499	0.0081	
$Ni_{35}Nb_{30}Zr_{15}Ti_{10}Fe_5Co_5$	Ribbon (30-60)	UC	SR5.73	50(1)	4.556	0.01	[21]
		Charged			4.318	0.0125	
$Ni_{45}Nb_{30}Zr_{25}$		UC			4.406	0.0146	
		Charged			3.908	0.0151	
$Ni_{33}Nb_{22}Zr_{40}Co_5$		UC			3.448	0.0212	
		Charged			4.801	0.0124	
$Ni_{27}Nb_{18}Zr_{50}Co_5$		UC			2.924	0.0234	
		Charged			4.528	0.0156	
$Zr_{46}Cu_{30.14}Ag_{8.36}Al_8Be_{7.5}$	C3	UC	SR11.1	200(5)	1.500	0.15±0.01	[22]
$Zr_{54.7}Cu_{28.598}Ag_{5.852}Al_{5.6}Be_{5.25}$		UC			1.189	0.2±0.02	
		A625(60)			1.258	0.29±0.02	
$Zr_{52.5}Cu_{17.9}Ni_{14.6}Al_{10}Ti_5$	C7	UC	SR31.5	300(0.5)	2.328	0.0173	[23]

				300(1)	2.415	0.0151	
				300(5)	2.542	0.0141	
				300(10)	2.996	0.0103	
				300(20)	3.039	0.0102	
			SR2.91	15(1)	3.631	0.0156	
		UC	SR5.75	60(1)	3.071	0.015	
$Zr_{52.5}Cu_{17.9}Ni_{14.6}Al_{10}Ti_5$	C7		SR31.5	300(1)	2.563	0.0151	[24]
			SR2.91	15(1)	3.650	0.0208	
		A630(60)	SR5.75	60(1)	4.402	0.0199	
		UC			2.954	0.0315	
$Zr_{52.5}Cu_{17.9}Ni_{14.6}Al_{10}Ti_5$	D8(1)	HPT10	B	4(0.5)	2.403	0.0273	[25]
		HPT20			2.602	0.0191	
		A(top)			3.118	0.065	
		A(mid)			3.157	0.073	
		A(bottom)			3.801	0.067	
$Zr_{52.5}Cu_{17.9}Ni_{14.6}Al_{10}Ti_5$	C7	B(top)	SR1.78	$0.05s^{-1}$	3.666	0.07	[26]
		B(mid)			3.313	0.072	
		B(bottom)			3.119	0.069	
		UC			3.160	0.071	
		A573(540)	SR1.78		3.580	0.072	
		A573(1260)			3.793	0.063	
		A573(10080)			3.947	0.066	
$Zr_{52.5}Cu_{17.9}Ni_{14.6}Al_{10}Ti_5$	C7	UC		$0.05s^{-1}$	3.365	0.068	[27]
		A573(540)	SR3.80		3.608	0.067	
		A573(1260)			3.747	0.071	
		A573(10080)			3.907	0.065	
				50(0.5)	2.973	0.018	
				50(1)	3.140	0.0172	
TiZrHfCuNiBe	C3	UC	SR5	50(5)	3.474	0.015	[28]
				50(10)	3.903	0.0143	
				50(50)	4.002	0.0137	